High Resolution Traction Force Microscopy Based on Experimental and Computational Advances

Benedikt Sabass,* Margaret L. Gardel,† Clare M. Waterman,† and Ulrich S. Schwarz*
*University of Heidelberg, Heidelberg, Germany; and †The Scripps Research Institute, La Jolla, California

ABSTRACT Cell adhesion and migration crucially depend on the transmission of actomyosin-generated forces through sites of focal adhesion to the extracellular matrix. Here we report experimental and computational advances in improving the resolution and reliability of traction force microscopy. First, we introduce the use of two differently colored nanobeads as fiducial markers in polyacrylamide gels and explain how the displacement field can be computationally extracted from the fluorescence data. Second, we present different improvements regarding standard methods for force reconstruction from the displacement field, which are the boundary element method, Fourier-transform traction cytometry, and traction reconstruction with point forces. Using extensive data simulation, we show that the spatial resolution of the boundary element method can be improved considerably by splitting the elastic field into near, intermediate, and far field. Fourier-transform traction cytometry requires considerably less computer time, but can achieve a comparable resolution only when combined with Wiener filtering or appropriate regularization schemes. Both methods tend to underestimate forces, especially at small adhesion sites. Traction reconstruction with point forces does not suffer from this limitation, but is only applicable with stationary and well-developed adhesion sites. Third, we combine these advances and for the first time reconstruct fibroblast traction with a spatial resolution of $\sim 1\ \mu$m.

INTRODUCTION

A growing body of evidence suggests that physical force plays a crucial role as regulator of many cellular processes, including cell adhesion and migration (1–5). In particular, the dynamics of establishing actomyosin-generated traction force in an elastic environment appears to be central for the way cells sense and react to mechanical properties of their environment. Therefore, measuring cellular traction forces on elastic substrates is an essential tool for studying the regulation of cell adhesion and migration in a quantitative way (6,7).

The method of traction force microscopy was pioneered by the seminal work of Harris and co-workers, who were the first to use thin flexible silicone sheets as a wrinkling assay that gave a qualitative measure for the mechanical activity of cells (8). For quantitative studies it is essential to suppress wrinkling, which was achieved first for thin films under prestress (9,10) and later for thick films attached to a cover slide (11,12). Today traction force microscopy on thick elastic substrates has become a standard procedure to reconstruct cellular traction forces. Usually the films are prepared from polyacrylamide (PAA) or polydimethylsiloxane (PDMS) coated with adhesive ligands like fibronectin or collagen. PAA has the advantage that its stiffness can be tuned easily over the physiologically relevant range from 100 Pa to 100 kPa (13–15). PDMS, which is hard to prepare with a bulk stiffness below 10 kPa, has the advantage that it can easily be micropatterned (16–18). An alternative to flat elastic substrates is the pillar assay—an array of microfabricated PDMS-pillars that deform easily under cellular traction due to their small diameter (19–22). Because each pillar is a localized force sensor, the pillar assay allows a simple, albeit spatially constrained readout of the forces. For cell adhesion which is not spatially confined, however, flat elastic substrates are the method of choice.

A setup for traction force microscopy on flat elastic substrates has to combine different experimental and computational techniques. In Fig. 1 *A*, we show a schematic representation of the situation of interest. A cell is adhering to a flat substrate and exerts force through its sites of adhesion (traction pattern in *red*). The resulting deformations in the substrate are tracked by monitoring the movement of embedded marker beads (displacement field in *blue*). For PAA, usually fluorescent microbeads are employed which are embedded near the surface of the gel. For PDMS, micropatterning can be used to create a pattern which is easily detected with phase contrast microscopy. The displacement field has to be extracted from a pair of images, one image showing the substrate as it has deformed under cell traction, and one reference image showing the undeformed substrate. In general, there are two ways to approach the image processing task: either one directly tracks the movement of the fiducial markers (particle tracking velocimetry, PTV), or one makes use of a cross-correlation function to derive the local motion statistically (particle image velocimetry, PIV). Next one has to reconstruct the cellular traction pattern from the displacement field. For synthetic substrates like PAA or PDMS, one can assume an elastic behavior which is

Submitted May 29, 2007, and accepted for publication August 14, 2007.

Address reprint requests to Ulrich S. Schwarz, Tel.: 49-6221-54-51254; E-mail: ulrich.schwarz@bioquant.uni-heidelberg.de.

Margaret L. Gardel's current address is Department of Physics, University of Chicago, Chicago, IL.

Clare M. Waterman's current address is National Heart, Lung and Blood Institute, National Institutes of Health, Bethesda, MD.

Editor: Elliot L. Elson.

0006-3495/08/01/207/14 $2.00

doi: 10.1529/biophysj.107.113670

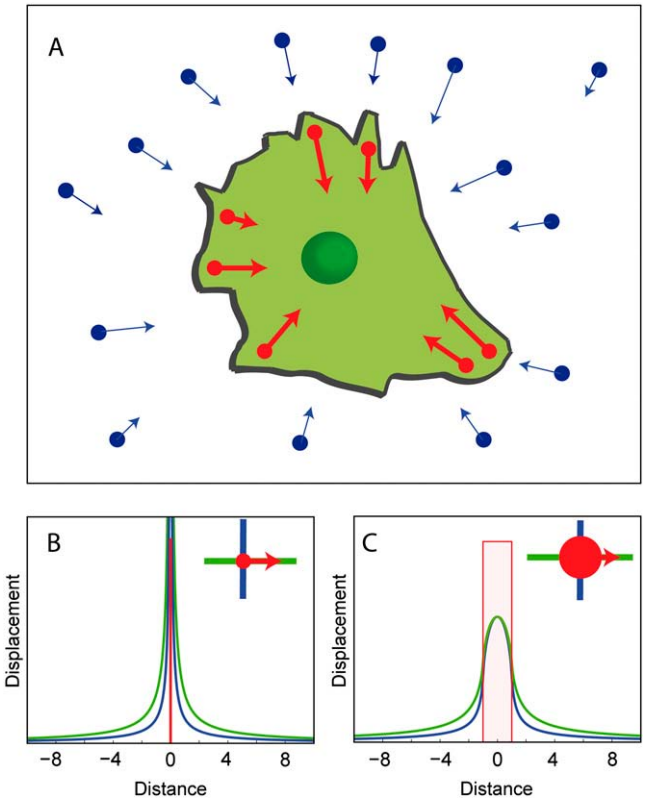

FIGURE 1 (*A*) Schematic representation of traction force microscopy on flat elastic substrates. Marker beads in the substrate and the corresponding displacement vector field are shown in blue. Sites of adhesion and the corresponding force vector field are shown in red. (*B*) If force is assumed to be strongly localized, one can use the concept of point forces, which leads to a divergent displacement field at the site of force application. Here we plot the magnitude of the displacement in two perpendicular directions. When relating force to displacement, the mathematical divergence can be avoided by using a simple cutoff rule. (*C*) If force is assumed to be spatially extended (here we show constant traction over a circular site of adhesion), then displacement is finite inside the adhesion area. Again we plot the magnitude of the displacement in two perpendicular directions. Traction of 2 kPa (2 nN/μm^2) at an adhesion of 2 μm in diameter corresponds to a maximum displacement of 0.3 μm on a 10 kPa substrate. At a distance larger than roughly twice the adhesion size, the displacements resulting from the two assumptions are identical.

homogeneous, isotropic, and linear. For cell adhesion in tissue culture, the cell is rather flat and force in the normal direction can be neglected. Then both the displacement field $\mathbf{u}(\mathbf{x})$ and the traction stress field $\mathbf{f}(\mathbf{x})$ are two-dimensional in the plane of the substrate (e.g., $\mathbf{x} = (x_1, x_2)$). They are related by the following integral equation:

$$u_i(\mathbf{x}) = \int \sum_j G_{ij}(\mathbf{x} - \mathbf{x}') f_j(\mathbf{x}') d\mathbf{x}'. \quad (1)$$

Given the experimental displacement $\mathbf{u}(\mathbf{x})$ and the relevant Green function $G_{ij}(\mathbf{x})$, one needs to invert Eq. 1 to obtain the desired traction field $\mathbf{f}(\mathbf{x})$. For thick films, the substrate can be approximated by an elastic half-space and thus one can use the Boussinesq Green function (23),

$$G_{ij}(\mathbf{x}) = \frac{(1+\nu)}{\pi E}\left[(1-\nu)\frac{\delta_{ij}}{r} + \nu\frac{x_i x_j}{r^3}\right] = \frac{(1+\nu)}{\pi E r^3}\begin{pmatrix} (1-\nu)r^2 + \nu x^2 & \nu xy \\ \nu xy & (1-\nu)r^2 + \nu y^2 \end{pmatrix}, \quad (2)$$

where ν and E represent Poisson ratio and Young modulus, respectively, and $r = |\mathbf{x}|$. For clarity, here we have written the Green tensor both in index notation and in full form. As it is typical for a three-dimensional elastic Green function, it scales as $\sim 1/r$ with distance, i.e., it is long-ranged and has a singularity at the origin. Thus, Eq. 1 is a Fredholm integral equation of the first kind with a weakly singular kernel. The long-ranged nature of the kernel implies that the direct problem corresponds to a smoothing operation. Therefore, the inverse problem might be very sensitive to small differences in the displacement field, depending on the exact nature of the experimental data. Noise in the experimental data can result from different sources, including elastic inhomogeneities in the substrate, insufficient coupling between marker beads and polymer matrix, deficiencies in the optical setup, and lack of accuracy in the tracking routines.

In the past, three standard methods have been established to calculate force from displacement. Both the boundary element method (BEM) (10,11) and the Fourier transform traction cytometry (FTTC) (24) approximate the integral on a grid (discretized methods). While BEM effectively corresponds to inverting a large system of linear equations in real space, FTTC uses the fact that the relevant system of linear equations is much smaller in Fourier space, thus facilitating inversion. Traction reconstruction with point forces (TRPF) (16,18,25) uses additional experimental knowledge about the location of the adhesion sites, which can be obtained for example by fluorescence data on proteins localizing to focal adhesions (e.g., vinculin or paxillin) (16,25) or by reflection interference contrast microscopy (18). Then the integral in Eq. 1 converts into a simple sum. In the past, there has been some dispute about advantages and disadvantages of these different methods. In particular, a priori it is not clear which of the two discretized methods performs better in respect to resolution and reliability. Moreover, different solutions have been suggested to deal with the issue of experimental noise, but a systematic and detailed analysis of the these approaches has been missing.

Here we present different experimental and computational advances which together allow us to achieve a much higher resolution and reliability in traction force microscopy than formerly possible. Experimentally we have implemented a new method to track the deformations of a PAA substrate by simultaneously using two differently colored nanobeads as fiducial markers. To extract the corresponding displacement field, we have developed a new image processing method combining PTV and PIV. Regarding the computational reconstruction of the traction field, we have implemented different variants of all three standard techniques (BEM,

FTTC, and TRPF) and systematically compared their performance using extensive data simulation. In particular, we have implemented an improved version of BEM and compared it to different new variants of FTTC. Analysis of simulated data revealed the importance of filtering for FTTC, and showed that certain variants of FTTC can perform almost as well as BEM while being much more efficient in terms of computer time demands. Both discretized methods are found to be strongly biased with respect to small adhesion sites. TRPF does not suffer from this limitation, but its underlying assumption of accurate knowledge of adhesion site location limits its applicability. Finally, we demonstrate with fibroblasts that our overall setup results in a spatial resolution which constitutes a 5–10-fold improvement over earlier methods.

EXPERIMENTAL METHODS

Cell culture

Mouse embryo fibroblasts were cultured in a humid environment at 37°C in 5% CO_2 in DMEM (cat. No. 10303; GIBCO BRL, Gaithersburg, MD) containing 10% fetal bovine serum (cat. No. 15630; GIBCO BRL). For experiments, cells were transfected with a plasmid encoding GFP-tagged paxillin (kind gift of A. R. Horwitz) using FuGENE 6 Transfection Reagent (cat. No. 11814443001; Roche, Nutley, NJ). After 12 h, cells were replated on the PAA substrates described below. Coverslips were mounted in a Warner Perfusion Chamber (Warner Instruments, Hamden, CT) and cells were imaged ~12–16 h after replating. Imaging media consisted of DMEM supplemented with 10 mM HEPES (GIBCO) pH 7.0 and Oxyrase (cat. No. EC0050; Oxyrase, Mansfield, OH).

Preparation of PAA substrates

We modified previously published protocols for making polyacrylamide substrates to maximize coupling of ECM and minimize variation between preparations. The surface chemistry of 22 × 40 mm rectangular, No. 1.5 glass coverslips (Corning, Corning, NY) was modified to facilitate a tight coupling of the PAA gel to the glass surface using protocols described by Wang and Pelham (26) and Damljanovic et al. (27). Briefly, coverslips are incubated in 0.5% 3-aminopropyltrimethyoxysilane (Pierce Biotechnology, Rockford, IL) for 5 min. After extensive rinsing, coverslips are then incubated in 0.5% glutaraldehyde solution (Electron Microscopy Sciences, Fort Washington, PA) for 30 min. After rinsing, coverslips are dried and stored for future use.

The 40% polyacrylamide and 2% bis-acrylamide solutions (Bio-Rad, Hercules, CA) were diluted to make stock solutions of 12% acrylamide/0.1% bis-acrylamide. Five-hundred milliliters of solution was degassed for 20 min under house vacuum and 0.75 μL of TEMED and 2.5 μL of 10% ammonium persulfate were added to initiate polymerization and mixed thoroughly. A volume of 20–25 μL of the polyacrylamide mixture was immediately pipetted onto the surface of a 22 × 80 mm glass slide and the activated coverslip was carefully placed on top. The polymerization is complete within 10–15 min and the top coverslip and attached polyacrylamide sheet were slowly peeled off and immediately immersed in ddH_2O. The ratio of TEMED and APS as well as the concentrations of acrylamide and bis were chosen to be identical to those published by Yeung et al. (15), such that we could use the values of the shear elastic modulus that they measured. The reported shear elastic modulus for the samples used here is 15.6 kPa. The thickness of the films varied between 20 and 30 μm.

The heterobifunctional cross-linker sulfo-SANPAH (cat. No. 22589, Pierce) is used to crosslink extracellular matrix molecules onto the gel surface. One-milligram aliquots of sulfo-SANPAH were stored at −80°C in 40 μL anhydrous DMSO and diluted in 1 mL ddH_20 immediately before coupling. The coverslips were quickly (<2 s) spun on a homemade coverslip spinner (http://www.proweb.org/kinesin/Methods/SpinnerBox.html) to eliminate the bulk of the water from the surface, but not dry out the gel. Five-hundred microliters of the sulfo-SANPAH solution was pipetted on the surface. The PAA gel was then placed three inches under a 10 W ultraviolet lamp and irradiated for 5 min at 4°C. It was then washed thoroughly with ddH_2O, spun and then inverted on 50 μL of 1 mg/mL Fibronectin (ChemiCon, Temecula, CA) for several hours at 4°C.

Live cell microscopy

Coverslips of cells were mounted in a microscope perfusion chamber (Warner Instruments) and imaged on a multispectral spinning disk confocal microscope similar to that described in Adams et al. (28), but with several upgrades. Briefly, the illumination system consisted of a 2.5 W water-cooled Innova 70c Krypton/Argon ion laser (Coherent, Santa Clara, CA) with the 488, 568, and 647 nm lines selected via a polychromatic acousto-optical modulator (Neos Technologies, Melbourne, FL) for excitation of GFP, x-rhodamine and cy-5, respectively. The laser illumination was delivered to the confocal scanhead (model No. CSU-10; Yokogawa, Tokyo, Japan) via a single mode optical fiber (Oz Optics, Ottawa, Ontario, Canada). The scanhead was equipped with a triple dichromatic mirror (Semrock, Rochester, NY) and bandpass emission filters (Semrock) mounted in a filterwheel apparatus (Sutter Instrument, Novato, CA) to allow capture of GFP, x-rhodamine, and cy-5 images in rapid succession. The scanhead was mounted on a model No. TE-2000E (Nikon, Tokyo, Japan) automated inverted microscope equipped with a Perfect Focus system (Nikon) to maintain focus at the PAA/cell interface to within ±20 nm over time and a linearly encoded robotic stage (Applied Scientific Instruments, Eugene, OR) to allow sequential analysis of cells at multiple stage positions. Temperature control was maintained on the microscope stage using an air curtain incubator (Nevtek, Burnsville, VA). Fluorescence images were generated with a 60× 1.2 NA Plan Apo water immersion objective lens (Nikon) using a 1.5× optovar. Triplets of images of GFP-Paxillin, 568/580 40-nm spheres, and 647/670 40-nm latex spheres were captured at 30-second intervals using a model No. HQ 2 camera (Roper, Sarasota, FL) equipped with an interline transfer CCD (6.4 μm pixel size) cooled to −30°C and operated in the 14 bit A/D mode. The exposure time is 0.5 s and therefore much smaller than the typical timescale on which cell traction changes (minutes). After imaging, cells were perfused with 2 mL of 0.5% trypsin to release cells from the PAA substrate, and an image of the unstrained substrate was taken in the 568 and 647 channels.

COMPUTATIONAL METHODS

Correlation-based particle tracking velocimetry

Extraction of a discrete displacement field describing the deformation of PAA substrates is done by comparing images before and after removal of the adhering cell with trypsin. For this purpose, we use a combination of particle image velocimetry (PIV) and particle tracking velocimetry (PTV) which we call correlation-based PTV. We acquire images of the fluorescent nanobeads at two different colors in two different channels of a spinning disk confocal microscope. In a first step, either of the images is partitioned into large windows (≈4–10 μm^2) and a standard PIV routine (29) is used to determine the deformation of the gel on a coarse scale. The result is used as an offset for the subsequent analysis and facilitates the detection of large deformations.

Subsequently, we use PTV and segment individual beads from both channels to gain higher resolution. Small windows (15×15 pix$^2 \approx 1$ μm^2) are placed on top of each bead before deformation $W_{\{c1,c2\}}(x,y)$ and compared with shifted windows after deformation $W^{d}_{\{c1,c2\}}(x+x',y+y')$. The indices c1, c2 indicate the different channels from which the images are taken. Tracking is done by maximizing the correlation of the mean-subtracted and normalized windows $\tilde{W}$:

$$\tilde{W}_{ci}(x,y) = \frac{W_{ci}(x,y) - \frac{1}{N}\sum_{x,y=1}^{N} W_{ci}(x,y)}{\sqrt{\sum_{x,y=1}^{N}\left(W_{ci}(x,y) - \frac{1}{N}\sum_{x,y=1}^{N} W_{ci}(x,y)\right)^2}}, \quad (3)$$

$$cc(x',y') = \frac{1}{2}\sum_{ci=\{c1,c2\}}\sum_{x,y=1}^{N} \tilde{W}^{d}_{ci}(x+x_0+x', y+y_0+y')\tilde{W}_{ci}(x,y), \quad (4)$$

where x_0 and y_0 are the offset values. The cross-correlation formula normalizes each window to a standard brightness and it is only the spatial contrast of the markers which is taken into account. Therefore changes in brightness of fluorescent marker beads (e.g., due to bead movement under traction, slight focus drift, or photobleaching) are not a problem. Note that by summing over the two channels, the correlation in both channels is maximized simultaneously. Mathematically, we avoid mixing terms in the cross correlation by averaging the correlation coefficients and not the windows themselves. The size of the windows, indicated by N, is a major factor for the distinctness of the global correlation peak. Therefore, we follow the suggestion of Ji and Danuser (30) and start with a small window size which we iteratively enlarge until a sufficient confidence level is reached. Subpixel accuracy is achieved by finding the maximum of the correlation matrix with the three-point Gaussian fit formula. For example, for the x-coordinate, it reads

$$x'^{subpix} = x' + \frac{ln[cc(x'-1,y')] - ln[cc(x'+1,y')]}{2\{ln[cc(x'+1,y')] + ln[cc(x'-1,y')] - 2ln[cc(x',y')]\}}. \quad (5)$$

This procedure yields precisions of ~0.2–0.4 pixel depending on the quality of images. Although peak locking was usually not observed, we nonetheless implemented a continuous window shift routine (31) for usage with densely covered and noisy images.

Boundary element method (BEM)

The BEM was the first method applied to quantitative traction force reconstruction on elastic substrates (10). The essential idea here is to discretize the integral in Eq. 1 on a computational mesh in such a way that the distance between two nodes is sufficiently small as to justify an interpolation between them. This permits us to carry out the integration with a bilinear interpolation scheme with the values of the traction at the nodes being still undetermined. First, a boundary for the computational mesh is established. The minimal choice is the cell boundary, but typically we fix the computational boundary outside the cell boundary to facilitate the discrimination of noise induced boundary effects from real traction. Then a node is created above each measured displacement which is located inside the computational boundary. Next, a triangular grid is produced with these nodes using Delaunay triangulation. During force reconstruction, extra nodes are added to produce a finer tessellation where needed. It is a particular useful feature of the BEM that the density of nodes can be increased at those locations where the force is localized.

As shown in the Appendix, Eq. 1 can now be written in matrix form:

$$u_{i\mathbf{x}} = \sum_{j}\sum_{\mathbf{x}'} M_{ij\mathbf{x}\mathbf{x}'} f_{j\mathbf{x}'}. \quad (6)$$

As it is typical for boundary element techniques, M is densely populated and ill-conditioned, thus making inversion time-consuming and difficult. To make the whole process more efficient, we have conceived a new method which splits the calculation of M into subroutines for near, intermediate and far fields. For the near field, the problem of a divergent integrand is remedied by using polar coordinates. Here, analytical integrals are calculated with the integration boundaries being determined by the position of the nearest triangles. The intermediate field, with a typical extension of five triangles in radial direction, is treated numerically with Gaussian quadrature in barycentric coordinates. The far field is evaluated analytically in the framework of a multipolar expansion. These three procedures are explained in more detail in the Appendix.

Even if the matrix M is calculated in this way, additional measures are required to arrive at a robust force estimate. The usual approach in the field of boundary element techniques is to implement a regularization scheme. This means constraining the solution to not only maximize its probability to estimate the experimental data in a least-square sense, but to also incorporate prior information about the expected traction field. We choose Tikhonov regularization and require the discrete field $f_{j\mathbf{x}'}$ to minimize the following target function:

$$\|u_{i\mathbf{x}} - \sum_{j,\mathbf{x}'} M_{ij\mathbf{x}\mathbf{x}'} f_{j\mathbf{x}'}\|^2 + \lambda^2 \|\sum_{j,\mathbf{x}'} L_{ij\mathbf{x}\mathbf{x}'} f_{j\mathbf{x}'}\|^2. \quad (7)$$

The simplest choice for L is the identity matrix (0^{th} order regularization). Constraining the amplitude of the solution with 0^{th} order regularization means suppressing high frequency and thus potentially noisy components in $f_{j\mathbf{x}'}$ (25). The prior information here is that the traction field is mostly located in small patches and zero elsewhere. Hence, sharp

peaks in the estimated solution are possible and will occur locally. Another choice for L is a discrete difference between the nodes (first-order regularization) (10,11). This choice is based on the assumption that the traction field is smooth rather than localized. Positive effects in regard to noise are similar to those with 0^{th} order regularization while traction plateaus are emphasized. For the numerical minimization of Eq. 7 we used the MatLab package Regularization Tools from Hansen (32). The regularization parameters were chosen using the L-curve criterion and a cross-validation Ansatz.

Fourier-transform traction cytometry (FTTC)

Fourier methods have been introduced for traction force reconstruction (24) because the convolution of Eq. 1 becomes a simple product in Fourier space. In detail, one has

$$\tilde{u}_{\mathbf{ik}} = \left\{ \sum_{\mathrm{j}} \tilde{G}_{\mathrm{ij}} \tilde{f}_{\mathrm{j}} \right\}_{\mathbf{k}}, \quad f_{\mathbf{ik}} = \left\{ \sum_{\mathrm{j}} \tilde{G}^{-1}_{\mathrm{ij}} \tilde{u}_{\mathrm{j}} \right\}_{\mathbf{k}}. \tag{8}$$

The Green function can be calculated from Eq. 2:

$$\begin{aligned} \tilde{G}_{\mathrm{ij}\mathbf{k}} &= \frac{2(1+\nu)}{E}\left[\frac{\delta_{\mathrm{ij}}}{k} - \frac{\nu k_{\mathrm{i}} k_{\mathrm{j}}}{k^3}\right] \\ &= \frac{2(1+\nu)}{Ek^3}\begin{pmatrix} (1-\nu)k^2 + \nu k_{\mathrm{y}}^2 & -\nu k_{\mathrm{x}} k_{\mathrm{y}} \\ -\nu k_{\mathrm{x}} k_{\mathrm{y}} & (1-\nu)k^2 + \nu k_{\mathrm{x}}^2 \end{pmatrix}. \end{aligned} \tag{9}$$

Again we give both index notation and the full form. Note that this tensor differs by an important minus sign in the off-diagonal elements from the formula printed in Butler et al. (24). The method proposed in that work proceeds as follows. The regular displacement field $u_{\mathbf{ix}}$ is smoothed using a frequency cutoff rule. Then it is transformed into Fourier space, multiplied with the inverse Green function, and the result is transformed back to real space. The transformations can be done with standard techniques for fast Fourier transform (FFT). The use of the FFT-algorithm to compute the Fourier transform of the displacement field $\tilde{u}_{\mathbf{ik}}$ requires a regular, rectangular grid covering the whole image, which is obtained from our irregular fields by biquadratic interpolation. We found that the adaptive Gaussian window technique performs rather badly in this context, because it is sensitive to the geometry of the given field. Note that the use of a regular rectangular grid is an important difference to the BEM-procedure, which uses irregular grids, which in turn allows locally adapting the node density.

In our work, we modified the FTTC suggested by Butler et al. (24) by testing different smoothing procedures for the displacement field, including an adaptive Wiener filter and a Gaussian filter. As an alternative approach, we removed the effects of noise directly from the calculated traction field. Here we choose, in analogy to the BEM, a regularization scheme and derive the corresponding variational equation:

$$\begin{aligned} &\iint \left[\sum_{\mathrm{l,j}} G_{\mathrm{li}}(\mathbf{x},\mathbf{x}'') G_{\mathrm{lj}}(\mathbf{x}'',\mathbf{x}') f_{\mathrm{j}}(\mathbf{x}') - \sum_{\mathrm{j}} G_{\mathrm{ji}}(\mathbf{x},\mathbf{x}'') u_{\mathrm{j}}(\mathbf{x}'') \right] d\mathbf{x}'' d\mathbf{x}' \\ &\quad + \lambda^2 \int \sum_{\mathrm{j}} H_{\mathrm{ji}}(\mathbf{x},\mathbf{x}') f_{\mathrm{j}}(\mathbf{x}') d\mathbf{x}' = 0. \end{aligned} \tag{10}$$

H is the square of L introduced above. This equation can now be transformed to Fourier space and solved there:

$$\tilde{f}_{\mathbf{ik}} = \left\{ \sum_{\mathrm{l,j}} \left[\sum_{\mathrm{m}} \tilde{G}_{\mathrm{ml}} \tilde{G}_{\mathrm{mi}} + \lambda^2 \tilde{H}_{\mathrm{il}} \right]^{-1} \tilde{G}_{\mathrm{jl}} \tilde{u}_{\mathrm{j}} \right\}_{\mathbf{k}}. \tag{11}$$

For the regularization kernel $H_{\mathrm{ij}}(\mathbf{x}, \mathbf{x}')$ we choose the identity matrix (0^{th} order regularization) or the square of an approximation for the Laplace operator (second-order regularization). The whole expression on the right-hand side of Eq. 11 can, like in the former method, be calculated at once, making the regularized method only marginally slower. The final step is, like above, the inverse Fourier transformation.

Traction reconstruction with point forces (TRPF)

Here we follow the procedure introduced by Schwarz et al. (25) for a traction microscopy study in which focal adhesions had been tagged with a fluorescent label. In brief, one assumes that all the traction is localized at discrete and known positions, i.e., the focal adhesions. Then the traction field is described by a sum of delta functions $f_{\mathrm{i}}(\mathbf{x}) = \sum_{\mathbf{x}'} F_{\mathbf{ix}'} \delta(\mathbf{x} - \mathbf{x}')$. This amounts to keeping only the first order term in a force multipolar expansion. The integral in the forward problem Eq. 1 is thus turned into a sum connecting each measured displacement to the set of force locations. The mathematical singularity has to be avoided by introducing a cutoff in which displacements closer to a point-force than approximately twice the typical size of a site of adhesion are ignored. One thus arrives, similar to the BEM, at a discrete, inverse problem where G is the Boussinesq solution in real space from Eq. 2:

$$u_{\mathbf{ix}} = \sum_{\mathrm{j},\mathbf{x}'} G_{\mathrm{ij}\mathbf{x}\mathbf{x}'} F_{\mathrm{j}\mathbf{x}'}. \tag{12}$$

This formula can be easily inverted by means of 0^{th} order Tikhonov regularization as described above for the BEM.

Simulated data: pointlike adhesions

To test the different variants of traction force microscopy described above, we used extensive data simulation. In general, we simulated both pointlike and spatially extended sites of adhesion. The difference in the resulting displacement fields is shown schematically in Fig. 1, *B* and *C*, respectively. For pointlike adhesions, we randomly distributed point forces over a finite region (the cell) and biased them to point to the center of this field (the cell body). The force

magnitudes were taken to fluctuate randomly in a given interval. For point forces, calculating the displacement field simply corresponds to the direct problem defined in Eq. 12. Displacement data was sampled from a random set of locations. Local displacement averaging was performed to mimic the effect of presmoothing by the correlation tracker on real data (window size 2 mesh sizes). Gaussian noise with a fixed standard deviation of 0–10% of the maximum displacement was added and then the traction force reconstruction was performed. Note that even for 0% noise, the reconstructed traction pattern will not reproduce the original traction pattern due to the different discretization steps involved.

Simulated data: finite-sized adhesions

We calculated an analytical solution for the strain field induced by a single circular adhesion with traction which is constant over the whole adhesion site, compare Fig. 1 *C*. Fourier transformation of the traction profile described by a two-dimensional step function yields a Bessel function of the first kind: $FT[f_j^0\Theta(r-R)] = f_j^0(2\pi R/k)J_1(kR)$. The displacement field was calculated by back-transforming the convolution with the Green function (9) into real space: $u_i(\mathbf{x}) = (1/2\pi)^2 \int(\sum_j \tilde{G}_{ij}\tilde{f}_j)(\mathbf{k})e^{-i\mathbf{kx}}d\mathbf{k}$. The resulting field is composed of hypergeometric functions and splits up into solutions for the inside and the outside of the adhesion. Use of the superposition principle permitted assembling artificial cells similar to the procedure described above for pointlike adhesions. In contrast to this case, however, now the individual adhesions not only differ in location and force magnitude, but also in size. The corresponding displacement fields were obtained as above for the pointlike adhesions by choosing random sites, averaging locally and addition of noise.

Dimensionless scores for quality of force reconstruction

All presented traction force routines were used on the test data. Optimization of filter parameters was done using a parameter scan and were then held constant for all samples at a given noise level. Three dimensionless scores were defined and measured to quantitatively assess the relative performance of the different methods.

Deviation of traction magnitude (DTM)

Relative difference of reconstructed and real traction magnitude summed over all adhesions:

$$DTM = \frac{1}{N}\sum_i \frac{\|\text{Reconstructed traction}\| - \|\text{Real traction}\|}{\|\text{Real traction}\|}. \tag{13}$$

N represents the number of adhesions and i runs over all adhesions. A negative DTM indicates that the measured tractions are too small, a positive DTM indicates that they are too large. The data on each adhesion is averaged before calculating the indicated norms.

Deviation of traction magnitude in the surrounding (DTMS)

Traction magnitude in a circular ring around the adhesions relative to the measured magnitude at the respective site:

$$DTMS = \frac{1}{N}\sum_i \frac{\|\text{Reconstructed traction in surrounding}\|}{\|\text{Reconstructed traction on adhesion}\|}. \tag{14}$$

Width of the ring was fixed to 1.5 mesh sizes. The DTMS quantifies the ability of different methods to reconstruct edges and contours, because for a successful reconstruction, the traction should decay rapidly outside the adhesion boundary. DTMS is expected to lie between 0 (optimal) and 1 (worst).

Deviation of traction angle (DTA)

Correlation of simulated traction and measured mean traction vector on adhesion:

$$DTA = \arccos\frac{1}{N}\sum_i \frac{\text{Reconstructed traction}\cdot\text{Real traction}}{\|\text{Reconstructed traction}\|\,\|\text{Real traction}\|}. \tag{15}$$

This definition corresponds to the difference in degree between the two (averaged) traction vectors.

RESULTS

Usage of two distinct kinds of fluorescent marker beads improves measured displacement field

The spatial resolution of the reconstructed traction field is directly related to the spatial resolution with which the displacement field is sampled. The use of a multispectral confocal spinning disk microscope permits acquisition of images from different fluorescence channels at high resolution (Fig. 2 *A*). To achieve an information content as high as possible, we used two differently colored beads densely embedded in the PAA gel. Fig. 2 *B* shows that the number of features is much higher if a combination of both channels is used. Fig. 2 *C* shows the tracking result for one channel. Open and solid circles indicate positions where beads could be only tracked by enlarging the correlation window (effectively lowering the spatial resolution) or not at all, respectively. Because the quality of images usually differs from channel to channel, it is impossible to interlace both extracted vector fields when tracking each channel by its own. Fig. 2 *D* shows the corresponding result for two channels obtained with the newly developed method of correlation-based PTV described above. Because the density of tracked displacements is now approximately twice as large, the mesh size determining spatial resolution is decreased by a factor of $\sqrt{2}$, from ~700 nm for

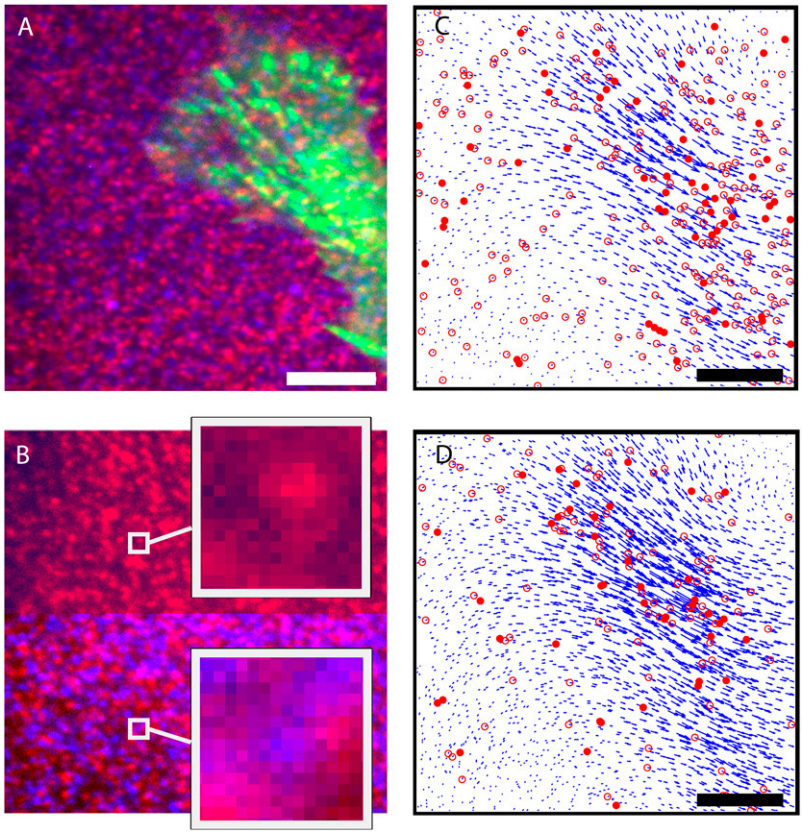

FIGURE 2 Extracting the displacement field from movement of two types of nanobeads with correlation-based particle tracking velocimetry. (*A*) The two different nanobeads (each with diameter 40 nm) are shown in red and blue. A fibroblast fluorescently marked with GFP-paxillin is shown in green. (*B*) Combination of both channels (*bottom*) shows more, but less distinct features than one channel alone (*top*). (*C*) Displacement field extracted from one channel only. Open circles at the base of an arrow indicate that this bead could only be tracked by enlarging the correlation window, effectively lowering the spatial resolution. Solid circles indicate beads which could not be tracked. The resulting mesh size is 700 nm. (*D*) Displacement field extracted from both channels simultaneously. Despite the displacement density being twice as high as in panel *C*, the number of enlarged windows and discarded beads is significantly lower. The resulting mesh size is 500 nm. Space bar 5 μm.

one channel to 500 nm for two channels. Thus our new method using two colors results in a much denser and more precise sampling of the displacement field than the traditional approach with one color only.

Spatial resolution of discretized methods strongly depends on traction magnitude and chosen filter

According to the Nyquist-Shannon sampling theorem, the optimal spatial resolution which can be achieved is determined by half the sampling frequency. For one- and two-channel tracking, this should be ~1.5 and 1 μm, respectively. To check whether this limit can be reached, we next investigated the capability of the different computational methods to distinguish very small traction sources. Resolution is defined by the Rayleigh criterion, i.e., as the minimum distance between two point forces at which they can still be separated. Fig. 3 *A* shows the chosen pattern of point forces (*red*) and the resulting displacement field (*blue*). Fig. 3, *B* and *C*, shows the results of the boundary element method (BEM) with 0^{th} and first-order regularization, respectively. Fig. 3, *D–G*, shows the results of Fourier-transform traction cytometry (FTTC) with four different treatments of noise (Gaussian filtering, Wiener filtering, 0^{th}, and second-order regularization, respectively). Visual inspection of this example demonstrates that very weak traction is not reproduced at all (marked with *solid arrows* in the original pattern, Fig. 3 *A*). The reconstructions from Fig. 3, *B–G*, also show that in several cases, close-by forces cannot be separated anymore (marked with *open arrows* in the reconstructions, Fig. 3, *B–G*). Yet all methods give a clear representation of the overall traction pattern, and strong point forces can always be distinguished clearly. Differences in resolution between BEM and FTTC were mainly due to mesh geometry and this gave the BEM a slight advantage. Moreover the choice of the filter procedure strongly influences point-force resolution. Qualitatively, those methods seem to work best for which no open arrows had to be added, that is, BEM with 0^{th} order regularization (Fig. 3 *B*), FTTC with Wiener filtering (Fig. 3 *E*), and FTTC with 0^{th} order regularization (Fig. 3 *F*). As indicated by the space bar (5 μm) in Fig. 3, in these cases we indeed reach a spatial resolution of 1 μm for displacement data corresponding to two-channel tracking.

To quantitatively determine the detection limit of the traction reconstruction, we generated 10 point force traction patterns and measured, for a substrate stiffness of $E = 10$ kPa, the reconstructed traction well outside the adhesion. These values are interpreted to represent a background in the traction pattern which potentially masks small forces. In Fig. 3 *H* we plot two times the standard deviation of this traction background as a function of the noise level (measured in absolute values, that is, pixel). This shows that increasing the noise level only leads to a slight increase in the detection limit. However, increasing the absolute level of the displacement

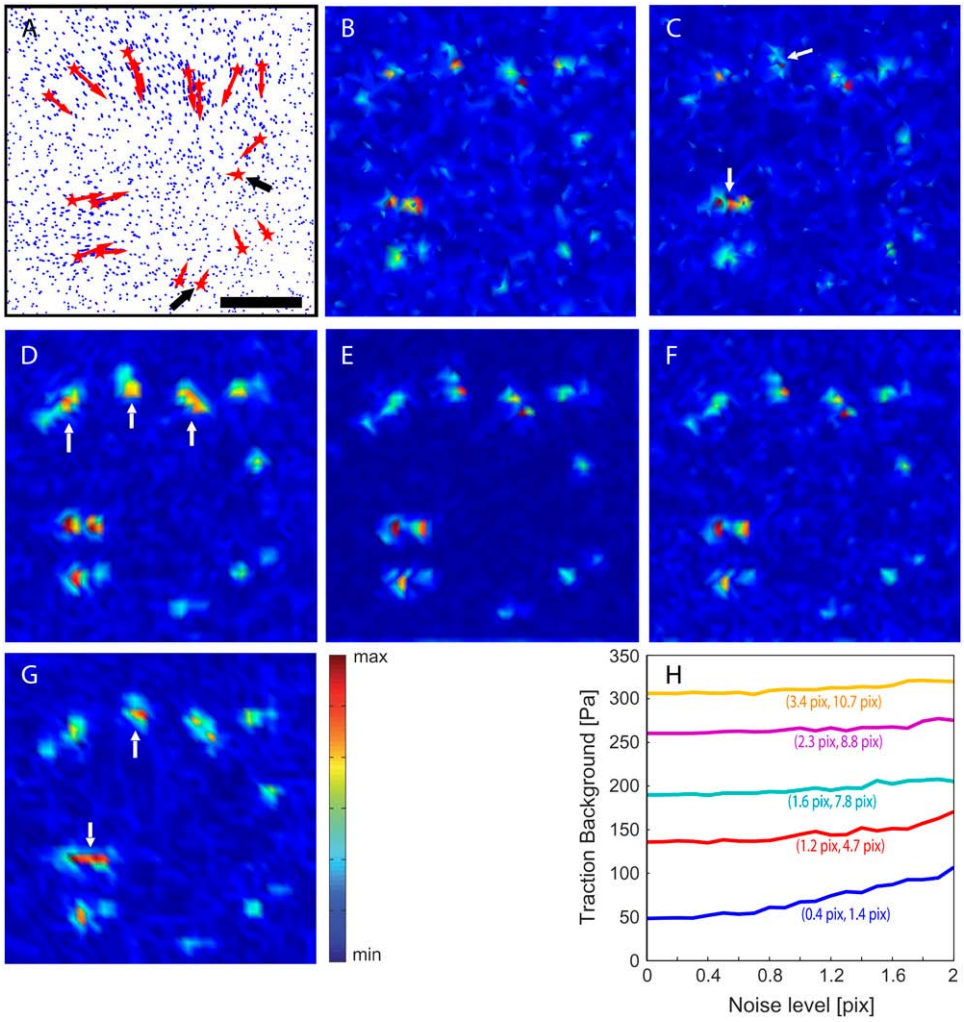

FIGURE 3 Reconstruction of traction at pointlike adhesions. (*A*) Random configuration of point forces (*red*) and resulting displacement field (*blue*). Space bar 10 mesh sizes (≈5 μm). (*B* and *C*) Reconstructed traction magnitude using the boundary element method (BEM). (*B*) BEM, 0^{th} order regularization. (*C*) BEM, first-order regularization. (*D–G*) Reconstructed traction magnitude using Fourier-transform traction cytometry (FTTC). (*D*) FTTC, Gaussian filter. (*E*) FTTC, Wiener filter. (*F*) FTTC, 0^{th} order regularization. (*G*) FTTC, second-order regularization. Solid arrows in panel *A* mark weak forces which cannot be detected at all. Open arrows mark positions where the reconstruction cannot distinguish between close-by forces in the original pattern. The performance is best for panels *B*, *E*, and *F*, with a spatial resolution of 1 μm. (*H*) Traction background is a statistical measure ($n = 10$) for the detection limit and is plotted here as a function of absolute noise (in pixel) for different absolute magnitudes of displacement (median and maximum value given in pixel). Traction background increases stronger with displacement magnitude than with noise.

field (represented by the median and maximum values in pixel) by increasing the original traction leads to a strong increase in the traction background. For example, for a maximum displacement of approximately eight pixels, the detection limit is ~200 Pa, corresponding to a force of 0.2 nN per μm^2. For the same displacement, but for a doubled substrate stiffness of $E = 20$ kPa, the traction background goes up by a factor of two, that is, to 400 Pa, corresponding to a force of 0.4 nN per μm^2. Therefore small forces cannot be resolved if the overall magnitude of traction is high, irrespective of the noise level.

BEM and FTTC produce comparable results

To arrive at a more general quantitative comparison between the different variants of traction force microscopy, we measured the three different scores defined in Computational Methods for circular adhesions with different noise levels in the displacement field. Our results are summarized in Table 1. For all three scores used (DTM, DTMS, and DTA), the closer its value to zero, the better the performance. In the absence of noise, filtering or regularization do not improve the results of FTTC. Here one sees that FTTC works comparably well to BEM with 0^{th} order regularization, but that BEM with first-order regularization is much worse. This result persists in the presence of noise, so in general BEM is best with 0^{th} order regularization. For FTTC, Table 1 shows that Wiener filtering is always better than Gaussian filtering and that 0^{th} order regularization is always better than second-order regularization. Moreover, Wiener filtering and 0^{th} order regularization perform equally well, and similar to BEM with 0^{th} order regularization. Thus these three methods indeed perform equally well, as suggested qualitatively by Fig. 3. However, there are dramatic difference in the required time for computation. While on a standard desktop computer BEM runs for several hours and requires large storage resources, FTTC only requires seconds. In addition, the programming effort is also highly reduced for FTTC, which can be encoded in a few pages whereas the BEM is, in our hands, spread out into more than a dozen subroutines. Thus FTTC with Wiener filtering or 0^{th} order regularization is both reliable and the most efficient choice in terms of resources.

TABLE 1 Quantitative performance of different variants of two standard methods in traction force microscopy, namely boundary element method (BEM), and Fourier-transform traction cytometry (FTTC)

		BEM with regularization		FTTC with filtering		FTTC with regularization	
Noise	Score	0^{th} order	First-order	Gaussian	Wiener	0^{th} order	Second-order
0%	DTM	−0.24 ± 0.19	−0.24 ± 0.20		−0.28 ± 0.19		
	DTMS	0.18 ± 0.06	0.24 ± 0.10		0.23 ± 0.02		
	DTA [°]	8.8	19.6		7.92		
5%	DTM	−0.47 ± 0.2	−0.59 ± 0.10	−0.55 ± 0.27	−0.43 ± 0.21	−0.48 ± 0.23	−0.47 ± 0.25
	DTMS	0.36 ± 0.09	0.56 ± 0.07	0.65 ± 0.16	0.37 ± 0.06	0.35 ± 0.04	0.42 ± 0.09
	DTA [°]	12.3	32.8	25.8	12.3	11.7	14.1
10%	DTM	−0.58 ± 0.14	−0.62 ± 0.16	−0.61 ± 0.25	−0.46 ± 0.22	−0.55 ± 0.2	−0.48 ± 0.25
	DTMS	0.50 ± 0.09	0.64 ± 0.17	0.86 ± 0.39	0.48 ± 0.12	0.48 ± 0.1	0.55 ± 0.18
	DTA [°]	17.4	33.0	32.2	19.9	17.6	23.2
Computation time		2–10 h			<2 s		

The three scores used are deviation of traction magnitude (DTM), deviation of traction magnitude in the surrounding (DTMS), and deviation of traction angle (DTA) ($n = 10$). In each case, the methods performs the better the closer the score is to zero. For BEM, 0^{th} order regularization works better than first-order regularization. For FTTC without noise, filtering or regularization does not improve the results. In the presence of noise, Wiener filtering works better than Gaussian filtering and 0^{th} order regularization works better than second-order regularization. Both Wiener filtering and 0^{th} order regularization perform similarly well, and comparable to BEM with 0^{th} order regularization. However, FTTC requires much less computation time. All computations were done on a single 2 GHz Pentium processor with 4 GB memory.

Traction magnitude of small adhesion sites is underestimated with discretized methods

Table 1 also shows that the deviation of traction magnitude (DTM) is always negative for both BEM and FTTC, thus significant underestimation of traction is a persistent challenge with the discretized methods. The causes of systematic and random underestimation are manifold but depend strongly on the sampling density of the displacement field, as suggested by the Nyquist criterion. Fig. 4 confirms this view and shows that the analysis of adhesion sites which are smaller than two mesh sizes is problematic. Fig. 4 *A* shows the original traction pattern with nine randomly placed circular adhesions (in *red*) and the resulting displacement field (in *blue*). Fig. 4, *B* and *C*, show traction force reconstruction with BEM with 0^{th} order regularization and FTTC with Wiener filtering, respectively. The difference between reconstructing traction on an irregular versus regular grid is clearly visible. In both cases, the overall traction pattern is nicely reproduced. In Fig. 4, *D* and *E*, the DTM is plotted as a function of adhesion size (measured in units of mesh size) for noise levels of 0 and 10%. Below a critical size, there is an inverse relation between DTM and adhesion size, meaning that force reconstruction is only reliable for large adhesions. For 0% noise, the critical value is approximately two mesh sizes, but shifts to larger values for higher noise levels. In the presence of 10% noise, only adhesions with a size approximately four times larger than the mesh size are reconstructed in a reliable way. For smaller adhesions, the DTM becomes strongly negative, thus the traction at these adhesions (and, concomitantly, the overall strain energies) are severely underestimated. In conclusion, it is critical to start with a dense sampling of the displacement field, because this results in small mesh sizes and thus in reliable force reconstruction for small adhesions and better estimates for strain energy.

Traction reconstruction with point forces is precise, but highly depends on correct localization of focal adhesions

To improve the force reconstruction at small adhesions, we employed traction reconstruction with point forces (TRPF), which explicitly starts from the assumption of highly localized force (25). Fig. 5 *A* shows a typical force reconstruction with TRPF (*green vectors*) from a displacement field with 10% noise (*blue vectors*). Fig. 5 *B* demonstrates that now the DTM depends much less on the size of the adhesion, resulting in a reliable force reconstruction over a large range of adhesion sizes. However, in this method it is critical that the localization of the adhesions is very precise. Fig. 5 *C* shows the results of the force reconstruction (*orange vectors*) if the sites of adhesion used for reconstruction have been deliberately misplaced in regard to the original sites of adhesion. The quantitative analysis using DTM and DTA in Fig. 5 *D* shows that directional errors and strong magnitude fluctuations occur if the adhesions are not placed well. This finding limits the applicability of the method to cells with few and distinct focal adhesions.

High resolution reconstruction for fibroblast traction

We finally demonstrate how the whole setup can be used to analyze fibroblast traction. Fig. 6 *A* shows an extension of a stationary mouse embryo fibroblast with discrete focal adhesions (marked by GFP-paxillin). To obtain the required

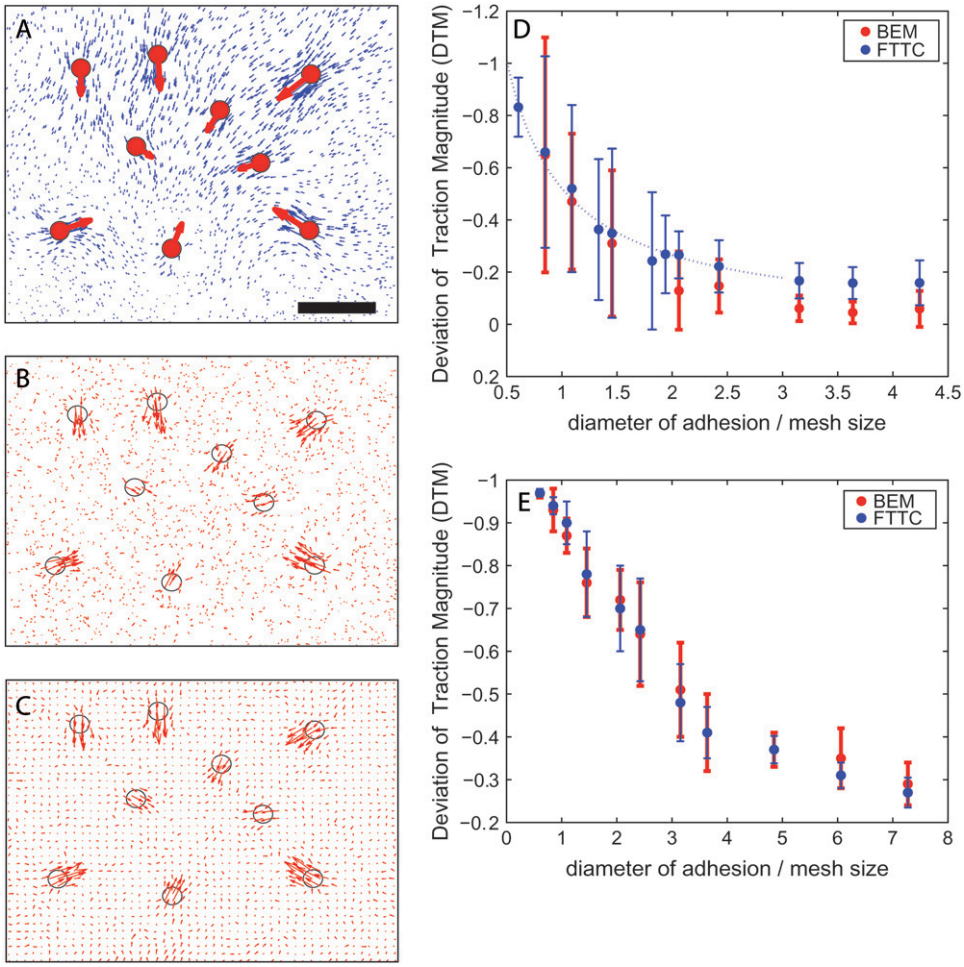

FIGURE 4 Reconstruction of traction at finite-sized adhesion sites. (*A*) Circular adhesion sites with constant traction (*red*) and resulting displacement field (*blue*). Space bar 10 mesh sizes (≈5 μm). (*B*) Traction reconstruction with BEM and 0^{th} order regularization for 5% noise. (*C*) Traction reconstruction with FTTC and Wiener filtering for 5% noise. (*D*) Deviation of traction magnitude (DTM) as a function of adhesion size (measured in units of mesh size) for 0% noise. DTM is optimal at zero and worst for −1 (complete underestimation) or +1 (complete overestimation). Here DTM is negative, i.e., the traction is systematically underestimated. The inverse scaling (*dotted line*) of magnitude deviation as a function of adhesion size indicates sampling problems for adhesion sites which are smaller than two mesh-sizes (~1 μm). (*E*) Same plot but with 10% noise. Necessary filtering shifts the effective sampling frequency and only adhesion sites larger than four mesh sizes (~2 μm) can be properly examined ($n = 10$).

spatial resolution for the displacement field, it is imperative to image only a limited region of the cell. Therefore we have chosen here a region of interest which does not have any additional close-by adhesions that might change the traction pattern inside the region of interest. Fig. 6 *B* shows an overlay with the displacement field extracted with two differently colored nanobeads. As explained above, the mesh size of ~500 nm results in a spatial resolution of ~1 μm because the computational reconstruction is combined with adequate filtering. For the substrate stiffness $E = 15.6$ kPa and the given fibroblast strength, the traction background is ~500 Pa, corresponding to a force of 0.5 nN per μm^2. In the reconstruction we often find forces of up to 10 kPa, corresponding to a force of 10 nN per μm^2, that is, 20-fold above the detection limit. Fig. 6, *C* and *D*, show the force vector fields obtained with BEM and FTTC, respectively, both with 0^{th} order regularization. Note that for the BEM the computational mesh is a irregular grid restricted to the wedgelike region including the cell contour. For FTTC, force vectors are reconstructed on a square lattice covering the whole image. In Fig. 6, *E* and *F*, we show color plots for the traction magnitudes for BEM and FTTC, respectively. Both methods give very similar results. In Fig. 6 *G* we show our results obtained with TRPF. In this case, first one point has been selected for each adhesion (for very large adhesions, two points have been selected). The resulting forces then show visual agreement with the results from BEM and FTTC. The direct comparison between the three different methods shown in Fig. 6 *H* for the small region marked in Fig. 6 *A* nicely summarizes the difference between the three methods: one force vector for TRPF, an irregular pattern for BEM, and a regular pattern for FTTC. In particular, it shows that the spatial resolution of BEM and FTTC is indeed ~1 μm.

DISCUSSION

This work aims at a thorough discussion of established and newly developed procedures to reconstruct cellular traction force on flat elastic substrates. In particular, we asked which approach will guarantee an optimal spatial resolution and magnitude reconstruction for different situations of interest. As an initial step, we extended the known experimental traction force protocols to the use of very small and differently colored fluorescent beads and a confocal microscope.

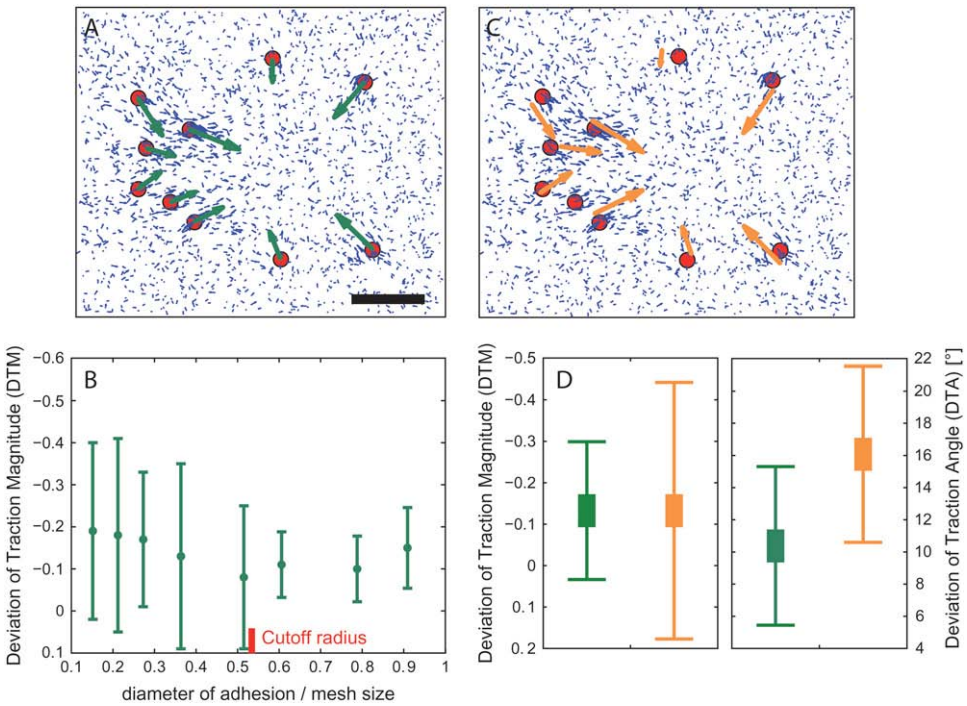

FIGURE 5 Traction reconstruction with point forces (TRPF). (*A*) Displacement field includes 10% noise. Point forces as calculated with TRPF (*green*) are localized in the center of adhesion sites (*red*). Space bar 10 mesh sizes (≈5 μm). (*B*) Deviation of traction magnitude (DTM) as a function of adhesion size as in Fig. 4, *D* and *E*. The underestimation of traction magnitude is small and does not depend strongly on adhesion size with TRPF. (*C*) Reconstruction of traction when point forces (*orange*) are not localized exactly in the center of adhesions, as it may occur with small and ill-defined adhesion sites. (*D*) Standard deviation of traction magnitude and directional error are much higher if point forces are not localized properly (*orange*) compared to correct localization (*green*) ($n = 10$).

The usage of two kinds of distinctly colored beads densely embedded in the gel permits the extraction of displacement fields with an average mesh size of 500 nm, setting the basic scale for the spatial resolution of the force reconstruction to 1 μm. This resolution is an improvement by a factor of ~5–10 compared with earlier work.

Cellular adhesion sizes vary considerably, ranging from a few hundred nanometers in nascent adhesions of locomoting cells to tens of microns for supermature focal adhesions in myofibroblasts. For small adhesions, the mesh size of the displacement data is larger than the adhesion feature size and thus the Nyquist frequency determining the theoretical upper limit for the resolution of traction forces is typically too low to capture all the details of the exerted traction field. Still one can ask which of the different computational methods performs best in reconstructing cellular traction fields. The main methods investigated here were BEM (10,11) and FTTC (24). For both methods, here we suggested different improvements, including analytical integration procedures and adaptive mesh generation for BEM and different filtering and regularization schemes for both BEM and FTTC.

An intrinsic feature of both methods is that solving the inverse stress-strain problem is equivalent to multiplying each Fourier component of the displacement field by its respective wave number. High frequency noise will thus be amplified and has to be removed while leaving as much as possible of the signal untouched. One can follow different philosophies here: physically, it seems reasonable to impose a smoothness constraint on the displacement field and filter it before the calculation of traction stress is performed. This technique only works with the Fourier transform methods. On the other hand, one can argue that it is better to choose a good solution a posteriori by inspection of its properties. Regularization constrains the resulting traction field and one can fine-tune it such as to compensate the above-mentioned effect of noise amplification to a desired level in the solution.

FTTC is seen to work best with Wiener filtering and 0^{th} order regularization in simulated data while experience with real data suggested that regularization is a more robust approach. BEM mostly work well with 0^{th} order regularization. An overall comparison of both approaches leads to the conclusion that FTTC, when combined with a proper filtering procedure, is in large parts comparable with BEM in regard to resolution. Initial advantages of the boundary element approach, resulting from the exact incorporation of irregular data, are lost in the presence of noise. Aliasing and boundary effects are not very prominent with boundary element methods, but can limit the performance of FTTC. The big advantage of FTTC is the very small run time compared with the BEM.

Both discretized methods suffer from a systematic underestimation of traction at small adhesion sites. It is thus interesting to ask whether traction force reconstruction with point forces (TRPF) can properly measure force magnitudes independent of adhesion size. The involved concept of a priori localized traction sources does, in fact, serve to avoid above bias. However, it is only applicable if the main assumption of this method, a reasonable localization of all traction sources, can be ensured. In general, traction measurement systems which do not permit the presumably force-mediated, yet temporary assembly of very small adhesion sites do seem to be a slightly ill-fated choice if the whole spectrum of forces and

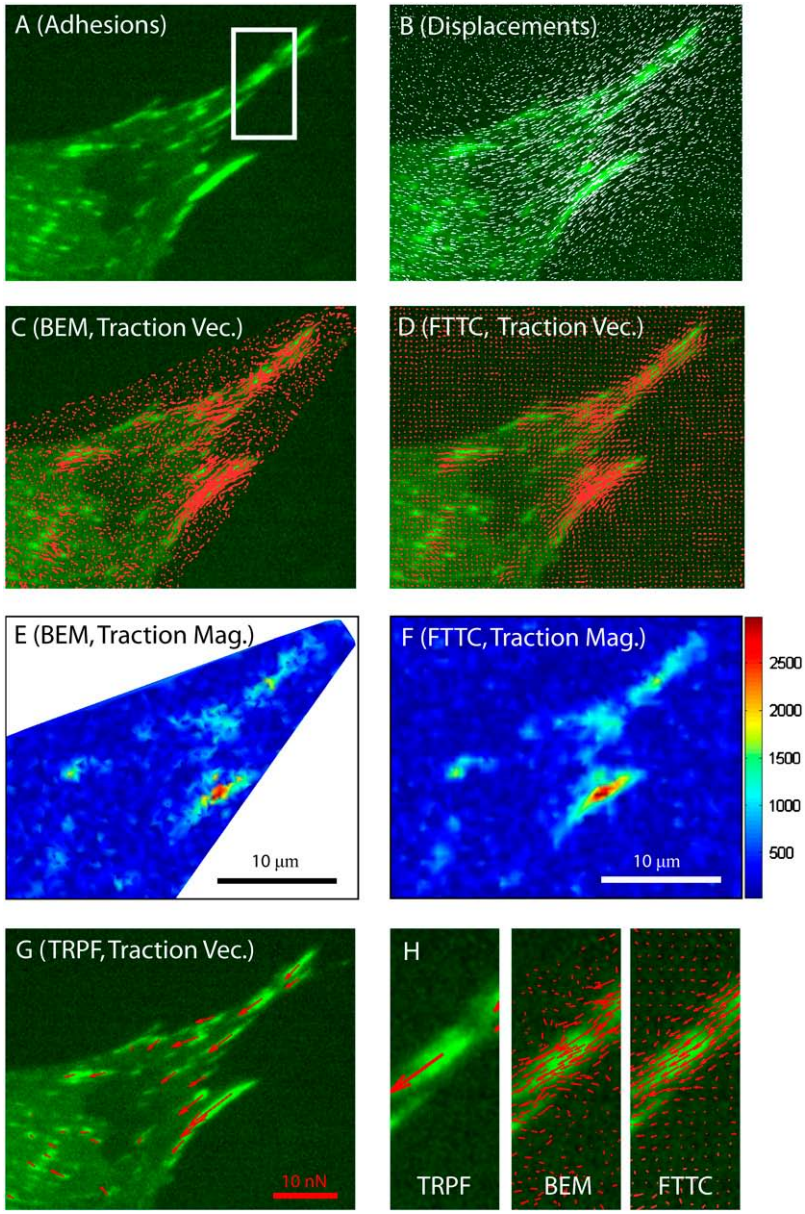

FIGURE 6 Traction forces at adhesions of a stationary fibroblast. (*A*) Image section of an extension of a fibroblast marked by GFP-paxillin (*green*). (*B*) Overlay with displacement field extracted with two differently colored nanobeads. (*C*) Traction vector reconstruction using BEM and 0^{th} order regularization. The computational mesh inside the wedge-shaped region is chosen such that the cell contour is well included. (*D*) Traction vector reconstruction using FTTC with 0^{th} order regularization. The computational mesh is a simple square lattice required for the FFTs. (*E*) Traction magnitude for the BEM-result. (*F*) Traction magnitude for the FTTC-result. Units of color bar given in Pascal. Both methods give similar results with a spatial resolution at ~1 μm and a lower bound for traction detection of ~500 Pa. (*G*) Traction vector reconstruction with TRPF. For each adhesion, one point has been selected (for very large adhesions, two points have been selected). (*H*) Comparison of TRPF, BEM, and FTTC for the region of interest marked in panel *A* around one large adhesion.

morphologies of cellular adhesion sites are to be studied in migrating cells.

Bearing in mind that several mechanisms may contribute to the force development at focal adhesions, a high spatial resolution is the sine qua non condition for a quantitative understanding of traction forces. From the work presented here, it is clear that dense displacement fields are the most important strategy to achieve this goal. Then a major drawback seems to be the concern that incorporating many marker beads in the gel contradicts the assumption of linear elasticity in the substrate. However, inclusions in an elastic material are known to perturb Young modulus and Poisson ratio only in a surrounding shell of the scale of the bead diameter (33). Therefore this effect might only be a problem when using large beads (e.g., microbeads).

In summary, our work shows that high resolution traction force microscopy relies on the combination of advances in substrate preparation, image processing, and computational force reconstruction. The systematic and quantitative comparison presented here shows that depending on the specific situation of interest and the resources at hand, different approaches are useful. For example, BEM with 0^{th} order regularization is the best choice to obtain high resolution traction patterns for migrating cells with many small adhesions and for small noise level in the displacement data. If computer time is a limiting factor, FTTC with 0^{th} order regularization is an almost equivalent alternative, especially at higher noise levels. For stationary cells in which focal adhesions can be well localized, TRPF is both computationally cheap and reliable.

APPENDIX: DETAILED DESCRIPTION OF THE BOUNDARY ELEMENT METHOD

The task is here to sequentially treat all possible interactions of tractions at nodes $\mathbf{x}'$ and displacements at $\mathbf{x}$. For brevity, in the following we use the Einstein sum convention. Traction interpolation between the nodes is done using triangular shape functions $P_{\mathbf{x}'_i}(\mathbf{x}_{\mathrm{tri}})$, where $\mathbf{x}_{\mathrm{tri}}$ symbolizes the continuous coordinates inside the triangle and $\mathbf{x}'_i$, $i \in \{1, 2, 3\}$ are the locations of its corners (nodes). Shape functions are defined in the usual way as the normalized area spanned by vectors connecting two of the corners $\mathbf{x}'$ with the point $\mathbf{x}_{\mathrm{tri}}$ and can thus be expressed as determinants:

$$P_{\mathbf{x}'_i}(\mathbf{x}_{\mathrm{tri}}) = \epsilon_{\mathrm{ijk}} \begin{vmatrix} \mathbf{x}_{\mathrm{tri}} & \mathbf{x}'_j & \mathbf{x}'_k \\ 1 & 1 & 1 \end{vmatrix} \Big/ \begin{vmatrix} \mathbf{x}'_1 & \mathbf{x}_2 & \mathbf{x}'_3 \\ 1 & 1 & 1 \end{vmatrix}. \tag{16}$$

Interpolation of traction is written in the following form: $f_j(\mathbf{x}_{\mathrm{tri}}) = P_{\mathbf{x}'_i}(\mathbf{x}_{\mathrm{tri}}) f_{j\mathbf{x}'_i}$. The discretized operator M, integral over the interpolation scheme, incorporates information about all the triangles surrounding the node $\mathbf{x}'_i$ in one matrix element:

$$M_{\mathrm{ij}\mathbf{x}\mathbf{x}'_i} = \sum_{\mathrm{triangles}} \int_{\Delta} G_{\mathrm{ij}}(\mathbf{x}, \mathbf{x}_{\mathrm{tri}}) P_{\mathbf{x}'_i}(\mathbf{x}_{\mathrm{tri}}) dx^2_{\mathrm{tri}}. \tag{17}$$

The computation time needed to loop through the combination of all nodes with all displacements can become intolerably long if high resolution is to be achieved with quadrature of Eq. 17. The exclusive use of numerical integration will thus demand for supercomputers or related facilities. Hence, we resort to a partial implementation of analytical integral results and also benefit from the high accuracy of this approach. The idea is here to compute the displacement field emanating from each triangular element, in analogy to a multipole field, depending on the distance. Separate subroutines were devised for three distinct cases.

Near field

Displacement is on top of the node. The Greens function diverges for $r = \|\mathbf{x} - \mathbf{x}'\| \to 0$. This difficulty is circumvented by usage of polar coordinates and the location of a node on top of each displacement. Any dependence of the Greens function from the distance is thus removed by the functional determinant:

$$\int_{\Delta} G_{\mathrm{ij}}(\mathbf{x}, \mathbf{x}_{\mathrm{tri}}) P_{\mathbf{x}'_i}(\mathbf{x}_{\mathrm{tri}}) dx^2_{\mathrm{tri}} = \int_0^{\varphi} \int_0^{R(\varphi)} (G_{\mathrm{ij}} r)(\varphi) P_{\mathbf{x}'_i}(r, \phi) dr d\varphi. \tag{18}$$

$R(\varphi)$ is an elementary trigonometric expression which, however, diverges for certain φ. This necessitates a coordinate rotation for each triangle in a preparatory step. The implementation of a precomputed, analytical integral solution makes the following evaluation very fast. The such calculated integral in the near-field is exact to the accuracy of the approximation by the triangulation.

Intermediate field

Displacement is in the surrounding of the node. Lack of better possibilities necessitates the use of Gaussian quadrature in this region. However, rewriting the integral to barycentric coordinates $(P_{\mathbf{x}'_1}, P_{\mathbf{x}'_2})$, i.e., usage of the shape functions as coordinates, facilitates the implementation:

$$\int_{\Delta} G_{\mathrm{ij}}(\mathbf{x}, \mathbf{x}_{\mathrm{tri}}) P_{\mathbf{x}'_i}(\mathbf{x}_{\mathrm{tri}}) dx^2_{\mathrm{tri}} = D \int_0^1 \int_0^{1-P_{\mathbf{x}'_2}} G_{\mathrm{ij}}(\mathbf{x}, P_{\mathbf{x}'_1}, P_{\mathbf{x}'_2}) P_{\mathbf{x}'_i} dP_{\mathbf{x}'_1} dP_{\mathbf{x}'_2}. \tag{19}$$

D is the functional determinant and equals the area of the parallelogram spanned by two of the triangle sides.

Far field

Displacement is far from the node. The integrand in Eq. 19 is expanded up to third order around the center of mass of the triangle ($\Delta P_i = P_{\mathbf{x}'_i} - \frac{1}{3}$):

$$G_{\mathrm{ij}}(\mathbf{x}, P_{\mathbf{x}'_1}, P_{\mathbf{x}'_2}) P_{\mathbf{x}'_i} \approx \sum_{n=0}^{3} \left[\frac{\partial}{\partial P_{\mathbf{x}'_1}} \Delta P_1 + \frac{\partial}{\partial P_{\mathbf{x}'_2}} \Delta P_2 \right]^n \frac{G_{\mathrm{ij}}(\mathbf{x}, P_{\mathbf{x}'_1}, P_{\mathbf{x}'_2}) P_{\mathbf{x}'_i}}{n!} \Bigg|_{P_{\mathbf{x}'} = \frac{1}{3}}. \tag{20}$$

This procedure leads to lengthy analytical terms which can be evaluated very quickly in a vectorized routine. The accuracy of the approximation for the integral mainly depends on the ratio of the dimensions of the triangle to the distance to the displacements. We found that ratios of 1:3–1:4 already lead to results which differ only by a very small percentage from the numerical values obtained with Gauss quadrature.

Profound gratitude is expressed by B.S. to Barbara Sabass for inspiration, encouragement, and support! The authors thank Timo Betz, Ke Hu, and Rudolf Merkel for helpful discussions.

U.S.S. was supported by the Emmy Noether Program of the German Research Foundation. B.S. and U.S.S. are supported by the Center for Modeling and Simulation in the Biosciences (BIOMS) at Heidelberg. M.L.G. is supported by the Jane Coffin Childs fund and a Burroughs Wellcome Career Awards at the Scientific Interface award. C.M.W. is supported by National Institutes of Health Director's Pioneer Award DP10D435 and American Heart Association Established Investigator 0640086N.

REFERENCES

1. Geiger, B., and A. Bershadsky. 2002. Exploring the neighborhood: adhesion-coupled cell mechanosensors. *Cell.* 110:139–142.
2. Discher, D. E., P. Janmey, and Y.-L. Wang. 2005. Tissue cells feel and respond to the stiffness of their substrate. *Science.* 310:1139–1143.
3. Orr, A. W., B. P. Helmke, B. R. Blackman, and M. A. Schwartz. 2006. Mechanisms of mechanotransduction. *Dev. Cell.* 10:11–20.
4. Vogel, V., and M. Sheetz. 2006. Local force and geometry sensing regulate cell functions. *Nat. Rev. Mol. Cell Biol.* 7:265–275.
5. Schwarz, U. S. 2007. Soft matters in cell adhesion: rigidity sensing on soft elastic substrates. *Soft Matter.* 3:263–266.
6. Beningo, K. A., and Y.-L. Wang. 2002. Flexible substrata for the detection of cellular traction forces. *Trends Cell Biol.* 12:79–84.
7. Roy, P., Z. Rajfur, P. Pomorski, and K. Jacobson. 2002. Microscope-based techniques to study cell adhesion and migration. *Nat. Cell Biol.* 4:E91–E96.
8. Harris, A. K., P. Wild, and D. Stopak. 1980. Silicone rubber substrata: a new wrinkle in the study of cell locomotion. *Science.* 208:177–179.
9. Lee, J., M. Leonard, T. Oliver, A. Ishihara, and K. Jacobson. 1994. Traction forces generated by locomoting keratocytes. *J. Cell Biol.* 127: 1957–1964.
10. Dembo, M., T. Oliver, A. Ishihara, and K. Jacobson. 1996. Imaging the traction stresses exerted by locomoting cells with the elastic substratum method. *Biophys. J.* 70:2008–2022.
11. Dembo, M., and Y.-L. Wang. 1999. Stresses at the cell-to-substrate interface during locomotion of fibroblasts. *Biophys. J.* 76:2307–2316.
12. Pelham, R. J., and Y.-L. Wang. 1999. High resolution detection of mechanical forces exerted by locomoting fibroblasts on the substrate. *Mol. Biol. Cell.* 10:935–945.
13. Engler, A., L. Bacakova, C. Newman, A. Hategan, M. Griffin, and D. Discher. 2004. Substrate compliance versus ligand density in cell on gel response. *Biophys. J.* 86:617–628.

14. Engler, A. J., L. Richert, J. Y. Wong, C. Picart, and D. E. Discher. 2004. Surface probe measurements of the elasticity of sectioned tissue, thin gels and polyelectrolyte multilayer films: correlations between substrate stiffness and cell adhesion. *Surf. Sci.* 570:142–154.

15. Yeung, T., P. C. Georges, L. A. Flanagan, B. Marg, M. Ortiz, M. Funaki, N. Zahir, W. Ming, V. Weaver, and P. A. Janmey. 2005. Effects of substrate stiffness on cell morphology, cytoskeletal structure, and adhesion. *Cell Motil. Cytoskeleton.* 60:24–34.

16. Balaban, N. Q., U. S. Schwarz, D. Riveline, P. Goichberg, G. Tzur, I. Sabanay, D. Mahalu, S. Safran, A. Bershadsky, L. Addadi, and B. Geiger. 2001. Force and focal adhesion assembly: a close relationship studied using elastic micro-patterned substrates. *Nat. Cell Biol.* 3:466–472.

17. Goffin, J. M., P. Pittet, G. Csucs, J. Lussi, J. J. Meister, and B. Hinz. 2006. Focal adhesion size controls tension-dependent recruitment of α-smooth muscle actin to stress fibers. *J. Cell Biol.* 172:259–268.

18. Cesa, C., N. Kirchgessner, D. Mayer, U. S. Schwarz, B. Hoffmann, and R. Merkel. 2007. Micropatterned silicone elastomer substrates for high resolution analysis of cellular force patterns. *Rev. Sci. Instrum.* 78: 034301.

19. Tan, J. L., J. Tien, D. M. Pirone, D. S. Gray, K. Bhadriraju, and C. S. Chen. 2003. Cells lying on a bed of microneedles: an approach to isolate mechanical force. *Proc. Natl. Acad. Sci. USA.* 100:1484–1489.

20. du Roure, O., A. Saez, A. Buguin, R. H. Austin, P. Chavrier, P. Silberzan, and B. Ladoux. 2005. Force mapping in epithelial cell migration. *Proc. Natl. Acad. Sci. USA.* 102:2390–05.

21. Cai, Y., N. Biais, G. Giannone, M. Tanase, G. Jiang, J. M. Hofman, C. H. Wiggins, P. Silberzan, A. Buguin, B. Ladoux, and M. P. Sheetz. 2006. Nonmuscle myosin IIa-dependent force inhibits cell spreading and drives F-actin flow. *Biophys. J.* 91:3907–3920.

22. Saez, A., M. Ghibaudo, A. Buguin, P. Silberzan, and B. Ladoux. 2007. Rigidity-driven growth and migration of epithelial cells on microstructured anisotropic substrates. *Proc. Natl. Acad. Sci. USA.* 104: 8281–8286.

23. Landau, L. D., and E. M. Lifshitz. 1970. Theory of elasticity. *In* Course of Theoretical Physics, Vol. 7, 2nd Ed. Pergamon Press, Oxford, UK.

24. Butler, J. P., I. M. Tolic-Norrelykke, B. Fabry, and J. J. Fredberg. 2002. Traction fields, moments, and strain energy that cells exert on their surroundings. *Am. J. Physiol. Cell Physiol.* 282:C595–C605.

25. Schwarz, U. S., N. Q. Balaban, D. Riveline, A. Bershadsky, B. Geiger, and S. A. Safran. 2002. Calculation of forces at focal adhesions from elastic substrate data: the effect of localized force and the need for regularization. *Biophys. J.* 83:1380–1394.

26. Wang, Y.-L., and R. J. Pelham. 1998. Preparation of a flexible, porous polyacrylamide substrate for mechanical studies of cultured cells. *Methods Enzymol.* 298:489–496.

27. Damljanovic, V., B. C. Lagerholm, and K. Jacobson. 2005. Bulk and micropatterned conjugation of extracellular matrix proteins to characterized polyacrylamide substrates for cell mechanotransduction assays. *Biotechniques.* 39:847–851.

28. Adams, M. C., W. C. Salmon, S. L. Gupton, C. S. Cohan, T. Wittmann, N. Prigozhina, and C. M. Waterman-Storer. 2003. A high-speed multispectral spinning-disk confocal microscope system for fluorescent speckle microscopy of living cells. *Methods.* 29:29–41.

29. Willert, C. E., and M. Gharib. 1991. Digital particle image velocimetry. *Exper. Fluids.* 10:181–193.

30. Ji, L., and G. Danuser. 2005. Tracking quasi-stationary flow of weak fluorescent signals by adaptive multi-frame correlation. *J. Microsc.* 222:150–167.

31. Gui, L., and S. T. Wereley. 2002. A correlation-based continuous window-shift technique to reduce the peak locking effect in digital PIV image evaluation. *Exper. Fluids.* 32:506–517.

32. Hansen, P. C. 1998. Rank-deficient and discrete ill-posed problems. *In* SIAM Monographs on Mathematical Modeling and Computation. SIAM, Philadelphia, PA.

33. Jasiuk, I., P. Sheng, and E. Tsuchida. 1997. A spherical inclusion in an elastic half-space under shear. *J. Appl. Mech.* 64:471–479.